CrossMark

Buffer effects on the mosaic structure of the HR-GaN grown on 6H-SiC substrate by MOCVD

Engin Arslan[1] · Mustafa K. Öztürk[2] · Engin Tıraş[3] · Tülay Tıraş[3] ·
Süleyman Özçelik[2] · Ekmel Özbay[1]

Abstract High-resistive GaN ($>10^8$ Ω cm) layers have been grown with different buffer structures on 6H-SiC substrate using metalorganic chemical vapor deposition reactor. Different combination of the GaN/AlN super lattice, low temperature AlN, high temperature AlN and $Al_xGa_{1-x}N$ (x ≈ 0.67) layers were used in the buffer structures. The growth parameters of the buffer layers were optimized for obtaining a high-resistive GaN epilayer. The mosaic structure parameters, such as lateral and vertical coherence lengths, tilt and twist angle (and heterogeneous strain), and dislocation densities (edge and screw dislocations) of the high-resistive GaN epilayers have been investigated using x-ray diffraction measurements. In addition, the residual stress behaviors in the high-resistive GaN epilayers were determined using both x-ray diffraction and Raman measurements. It was found that the buffer structures between the HR-GaN and SiC substrate have been found to have significant effect on the surface morphology and the mosaic structures parameters. On the other hand, both XRD and Raman results confirmed that there is low residual stress in the high-resistive GaN epilayers grown on different buffer structures.

✉ Engin Arslan
engina@bilkent.edu.tr

1   Department of Physics, Department of Electrical and Electronics Engineering, Nanotechnology Research Center-NANOTAM, Bilkent University, 06800 Ankara, Turkey

2   Department of Physics, Faculty of Science and Arts, Gazi University, Teknikokullar, 06500 Ankara, Turkey

3   Department of Physics, Faculty of Science, Anadolu University, Yunus Emre Campus, 26470 Eskisehir, Turkey

1 Introduction

Because of the high-electron drift velocities and large dielectric breakdown voltage, III-nitride based heterojunction field effect transistor (HFET) devices have significant advantages for high power, high frequency applications operation [1–3].

The prevention of the current path underneath the two-dimensional electron gas (2DEG) channel and also complete channel pinch-off, low loss at high frequencies, and low cross-talk between adjacent devices can be satisfied by using a high-resistive (HR) or semi-insulating (SI) GaN channel layer in the high electron mobility transistor (HEMT) structures [4–6]. During the GaN layer growth, high unintentional n-type doping levels presumably doping due to the residual oxygen or silicon donors introduced to the structures. Intrinsic n-type conductivity may be adequate for light-emitting devices, such as light emitting diode and laser diode, but it is detrimental for high-power/high-frequency device applications [2–6]. In order to compensate n-type conductivity and obtain semi-insulating and/or highly resistive materials acceptors or acceptor like states are usually introduced to the structures [7–12]. In the GaN epilayer, the residual donors have to be compensated by acceptor states. Commonly, this is achieved by doping acceptor-like impurities, such as iron [7], magnesium [8], or carbon [9] during the growth of the GaN layer or by introducing high densities of threading dislocations [10] or by choosing growth conditions that result in high levels of carbon impurities, thereby leading to the formation of deep acceptor states [11–13]. Carbon incorporation in GaN has found important practical application in forming semi-insulating and/or highly resistive layers [11–13]. The carbon level and, as a result of this doping, the resistivity of the GaN layer can be easily controlled by varying the growth

temperature, deposition chamber's pressure, and V/III ratio [11–13].

Another important point for the growth of the HR-GaN layer is the buffer structures. In the MOCVD growth, the buffer layers used between the 6H-SiC substrate and the GaN layer strongly effect the crystal quality and electrical properties of the GaN layer [14–16]. Chen et al. [6] showed that the AlGaN layer between the AlN buffer and the GaN layer decreases the Si atoms density in the structures and hence changed the resistivity of the GaN layer. In the study of Twigg et al. [10], they showed that the AlN nucleation layer can strongly influence the resistivity of the subsequent GaN.

In our study, we obtained HR-GaN layers ($>10^8$ Ω cm) using different buffer structures, such as low temperature growth AlN, high temperature growth AlN, undoped AlGaN layer, and AlN/GaN superlattice between the 6H-SiC substrate and GaN layer. The structures were grown by MOCVD system. In the second part of the study, the mosaic model was used to describe the microstructure of the HR-GaN layer and calculated the mosaic structures parameters, such as lateral and vertical coherence lengths (average size of the mosaic blocks) tilt and twist angle, heterogeneous strain, and dislocation densities (edge and screw dislocations). The mosaic structure features and residual stress state of hexagonal HR-GaN layers were determined by x-ray diffraction (XRD) measurements. Raman scattering has been extensively used to evaluate stress form in the GaN based materials. Stress in the GaN layers are the important factor that changes the energy band structure and can influence the properties of the phonon modes. The frequency of the E_2 (high) phonon modes in GaN is sensitive to the residual stress. The E_2 (high) is the usable mode for accurate determination of the stress form in GaN structures. In this report, the stress form in hexagonal GaN using the E_2 (high) phonon modes, which are observed in Raman experiments performed in the backscattering geometry perpendicular to the surface. The resistivity's of the GaN layers were measured with a Hall measurements system at room temperature. Additionally, atomic force microscopy (AFM) imaging was performed in order to obtain detailed knowledge on the surface morphology of the samples.

2 Experimental procedure

The HR-GaN layers were grown on 6H-SiC substrates, with different buffer layers structures, in a low-pressure MOCVD reactor (Aixtron 200/4 HT-S) by using trimethylgallium (TMGa), trimethylaluminum (TMAl), and ammonia as Ga, Al, and N precursors, respectively. The growth procedure has been begun with surface baking of the SiC substrate under H_2 ambient at 1200 °C for

10 min. Four different sets of samples were grown with different buffer structures and named as sample A, B, C, and D after that. All of the samples nominally contain a 1.9 µm thick GaN epilayer after the buffer layers (Fig. 1). Sample A contains 10 nm thick LT-AlN, 140 nm HT-AlN, and 5×10 nm pairs GaN/AlN super lattice structures under the HR-GaN layer. In sample B, 10 nm LT-AlN and 140 nm HT-AlN layers were grown as a buffer layer. The buffer structures of the sample C consisted of a 10 nm thick, low-temperature (705 °C) AlN (LT-AlN) nucleation layer, and 230 nm thick undoped AlGaN layer. XRD peak splitting was used to measure the Al content of the AlGaN layer and its value found as 67 %. And 300 nm thick high-temperature AlN (HT-AlN) grown at 1100 °C were used as a buffer layer in sample D. A Ti/Al/Ni/Au metal stack was used as an ohmic contact in square Van der Pauw geometry for electrical characterization.
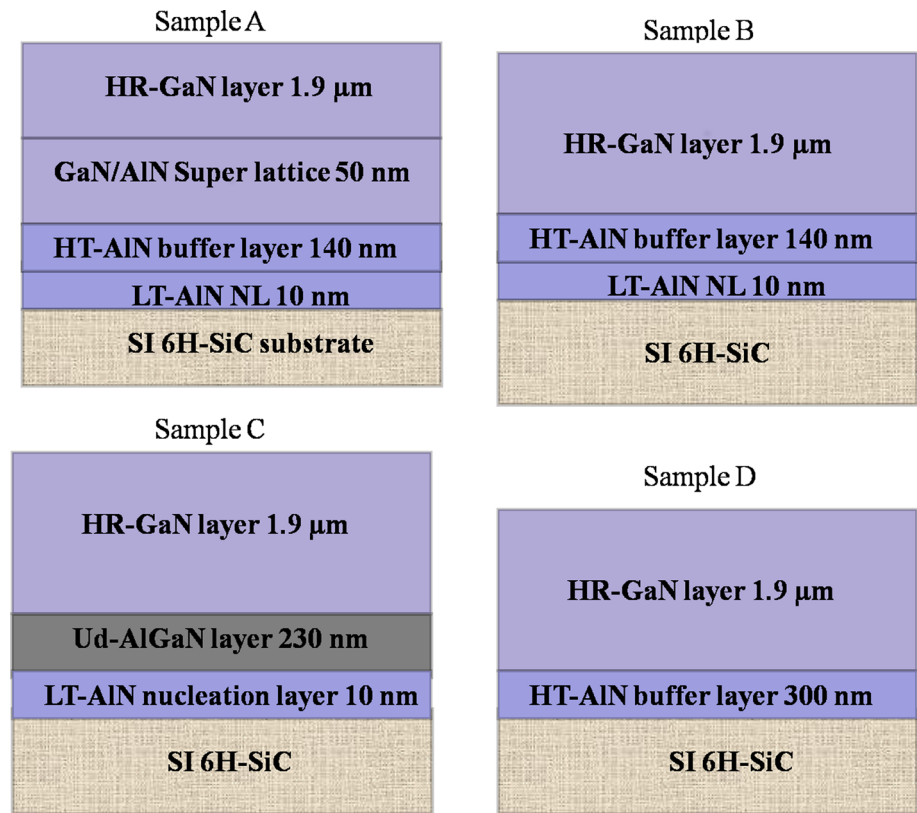
The resistance of the samples was measured at the room temperature by Hall measurements system. For x-ray diffraction measurements, a Rigaku Smart Lab. high-resolution diffractometer system, delivering CuKα1 (1.544 Å) radiation, and 4-bounce Ge(220) symmetric monochromator, was used. The Raman spectra's were recorded by using a Bruker Optics FT-Raman Scope III system. A 532 nm wavelength laser were used as an excitation source. All measurements were performed in backscattering geometry with the z-direction parallel to the c axis of the wurtzite GaN structure at room temperature. The samples' surface morphology was characterized by Atomic force microscopy (AFM) in contact mode with a commercial VEECO CPII.

3 Results and discussion

The surface morphology and root-mean-square roughness (RMS) of the HR-GaN layers grown on 6H-SiC substrate with different buffer layer structures is characterized by AFM over a 4.55×4.55 µm² scan size (Fig. 2). The AFM images of the HR-GaN layers in sample B, C and D exhibit step-flow growth and the terrace. However, some morphological defects are seen in the sample A. The RMS roughness values for samples are changed between 1.87 nm (for sample A) and 0.31 nm (for sample C). On the other hand, 0.48 and 0.84 nm RMS roughness values were obtained for sample B and sample D, respectively.

In the study, the growth parameters and thickness of the buffer layers were optimized for obtaining maximum resistivity for GaN layers. The resistivity of the samples was measured using square Van der Pauw geometry in a Hall measurements system at room temperature. The measured resistivity values of the GaN layers in all the samples are greater than 10^8 Ω cm.

Fig. 1 Schematic drawing of the HR-GaN epilayers grown on SI 6H-SiC substrate with different buffer structures

Sample A

| HR-GaN layer 1.9 μm |
| GaN/AlN Super lattice 50 nm |
| HT-AlN buffer layer 140 nm |
| LT-AlN NL 10 nm |
| SI 6H-SiC substrate |

Sample B

| HR-GaN layer 1.9 μm |
| HT-AlN buffer layer 140 nm |
| LT-AlN NL 10 nm |
| SI 6H-SiC |

Sample C

| HR-GaN layer 1.9 μm |
| Ud-AlGaN layer 230 nm |
| LT-AlN nucleation layer 10 nm |
| SI 6H-SiC |

Sample D

| HR-GaN layer 1.9 μm |
| HT-AlN buffer layer 300 nm |
| SI 6H-SiC |

Fig. 2 AFM images ($4.55 \times 4.55\ \mu m^2$ scans) of GaN epilayers in sample A, sample B, sample C and sample D

Sample A

Sample B
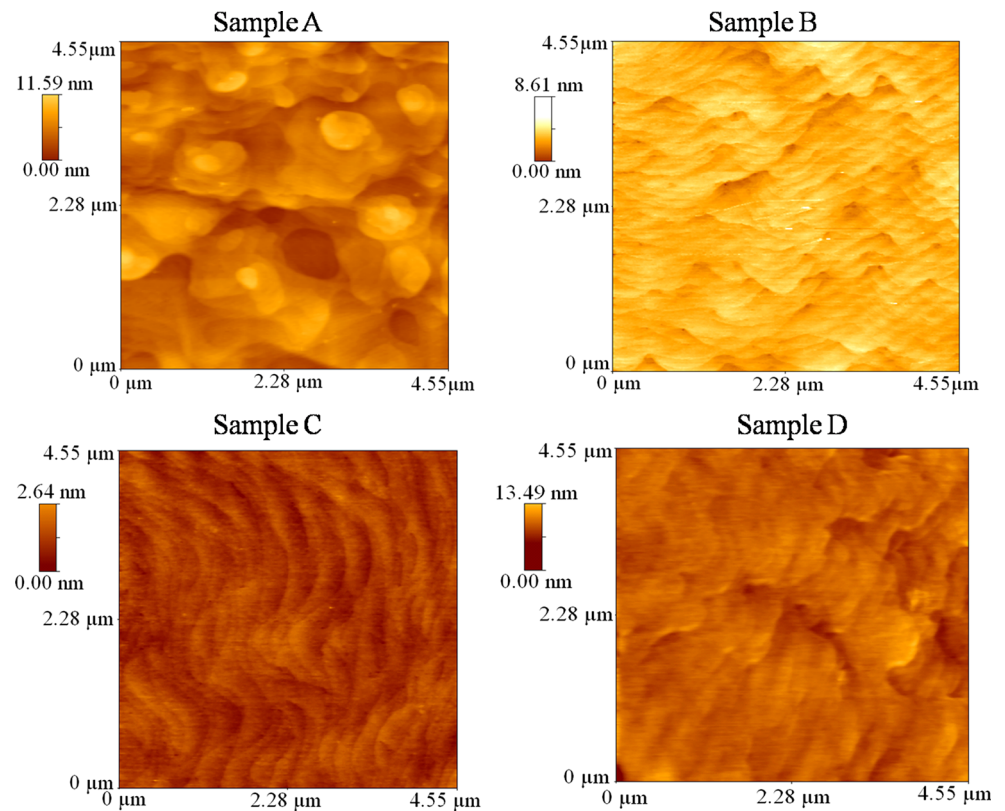
Sample C

Sample D

The XRD ω-2θ-scans were performed for all of the samples to investigate the crystal phase of the layers grown on 6H-SiC substrate and are shown in Fig. 3. The diffraction patterns exhibited the (0002) peaks of the wurtzite GaN, AlN, AlGaN epilayer, and 6H-SiC substrate. The (0002) peaks of the wurtzite GaN epilayers are clearly observed at 34.67°, 34.64°, 34.66°, and 34.61° for samples A, B, C, and D, respectively. In addition, peaks of the (0006) plane from the 6H-SiC substrate were measured at 35.68° for all the samples. An in-plane Φ-scan was also taken by rotating the sample around its surface-normal direction in order to investigate the in-plane alignment of GaN epilayer. The Φ-scan pattern of the (10–11) plane for sample C is given in Fig. 4. As can be seen from the figure, that the diffraction peaks from the (10–11) plane of GaN epilayers were observed at 60° intervals, which clearly confirms that the GaN epilayer have good single crystal hexagonal characteristics.

In order to precisely determine the lattice constants (a and c) of the hexagonal GaN crystal, the symmetric and skew symmetric XRD 2θ/ω-scans can be used in Eq. (1) with combining Bragg's law ($n\lambda = 2d_{hkl} \sin \theta$) [17–19].

$$d_{hkl} = 1/\sqrt{\frac{4}{3}\frac{h^2 + k^2 + hk}{a^2} + \frac{l^2}{c^2}} \quad (1)$$

Because of two unknowns (a and c) in Eq. (1), at least two different plane reflections (d_{hkl}) measurements are needed [17–19].The symmetric and skew symmetric ω-2θ scans for all basic crystallographic directions were measured. Generally, lattice constants c of the layer perpendicular to the interface are calculated from the one or two high-angle symmetric (000l) reflections such as (0004), (0006), and (0008) plane measurements. On the other hand, the lattice constants a parallel to the film interface can be
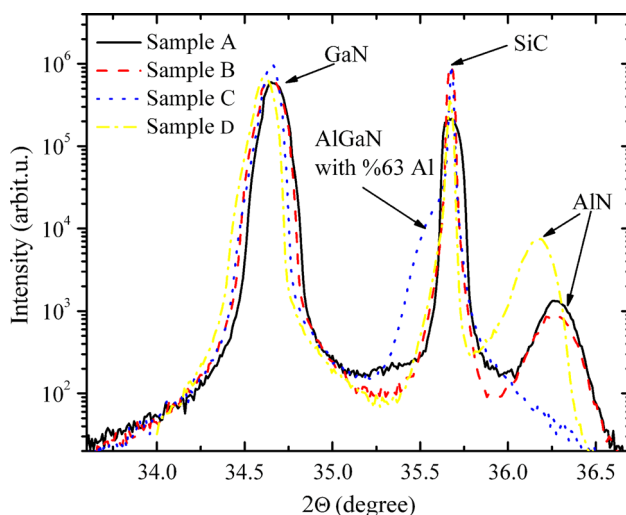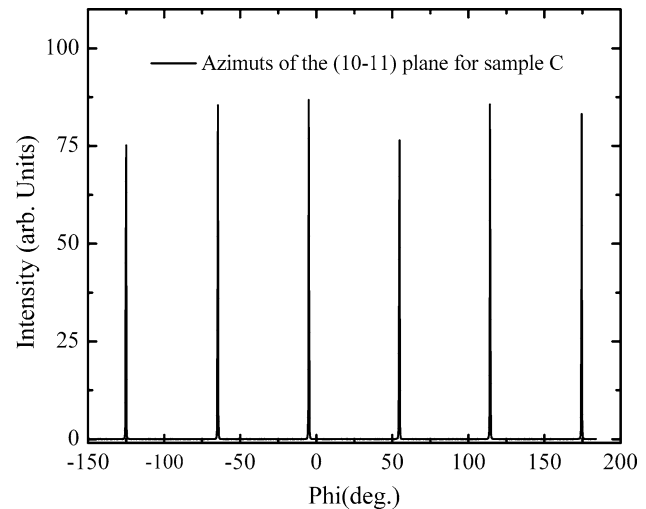
Fig. 4 Phi scan pattern of asymmetric (10–11) plane of the GaN epilayer for sample C. Every peak shows azimuths of the (10–11) plane

derived using the one or two diffraction peaks of the high-angle asymmetrical reflections, such as (10–14), (11–24), (10–15), and (20–24) [17–19]. In this study, the c and a values calculated from the (0004), (0006) symmetric plane reflections, and (10–12), (10–13), (10–14), and (20–21) asymmetric plane reflections measurements, respectively. Table 1 shows the calculated a and c values for all samples.

As it is known, the crystal system of the GaN is the wurtzite hexagonal [17–21]. When a GaN epitaxial layer is grown on a SiC substrate it is form a columnar mosaic structure [17–19]. The axes of the hexagonal shape columns is coincide with the crystallographic c-axis of GaN film and these columns are oriented about the c-direction of the SiC substrate with an effective small angle of about a few arcminutes. In the mosaic structures of the GaN film, the a and b crystallographic axes of the columns are perpendicular to the c-direction of the substrate. For this reason, the GaN epilayer exhibits in-plane isotropic elastic properties, and its in-plane deformation state can be described by one strain component. Therefore, in-plane strain (ε_a) and out-of-plane (ε_c) strain components of the GaN epilayers can be calculated by the equations given below [17–21],

$$\varepsilon_a = (a_{meas} - a_0)/a_0 \quad (2a)$$

$$\varepsilon_c = (c_{meas} - c_0)/c_0 \quad (2b)$$

In the Eqs. (2a) and (2b), c_{meas} and a_{meas} are the measured lattice constants of GaN and c_0 and a_0 are reference values for stoichiometric and defect-free unstrained GaN crystals ($c_0^{GaN} = 0.51855$ and $a_0^{GaN} = 0.31891$ nm [22]). However, the GaN epilayer in the heteroepitaxial GaN/buffer/substrate structures grown by the MOCVD method contains a high concentration of point defects that cause a considerable contraction or expansion (depending on the

Fig. 3 The ω-2θ XRD pattern of the HR-GaN epilayers grown on 6H-SiC substrate with different buffer structures

Table 1 The lattice parameters a_{meas}, c_{meas}, strains, biaxial stress and Raman frequency of the E_2 (high) phonon modes in HR-GaN/buffer/6H-SiC heteroepitaxial structures

Sample ID	a_{meas} ±0.00002 (nm)	c_{meas} ±0.00002 (nm)	Raman frequency of E_2 (high) phonon mode (cm^{-1})	FWHM of E_2 (high) phonon mode (cm^{-1})	Measured strain in a-direction, $\varepsilon_a \times 10^{-3}$ ± 2 × 10^{-4}	Measured strain in c-direction, $\varepsilon_c \times 10^{-3}$ ± 1 × 10^{-4}	Hydrostatic strain, $\varepsilon_h \times 10^{-3}$ ± 2 × 10^{-4}	Biaxial strain in a-direction, $\varepsilon_a^b \times 10^{-4}$ ± 1 × 10^{-5}	Biaxial strain in c-direction, $\varepsilon_c^b \times 10^{-4}$ ± 1 × 10^{-5}	Biaxial stress, σ_f (GPa) × 10^{-2} ± 1.4 × 10^{-3}
Sample A	0.31958	0.51972	566.6	4.9	2.1	2.2	2.2	−1.0	0.5	−4.8
Sample B	0.31968	0.51976	566.1	3.4	2.4	2.3	2.4	0.5	−0.3	2.5
Sample C	0.31899	0.51873	566.0	3.3	0.25	0.3	0.3	−0.6	0.3	−3.0
Sample D	0.31918	0.51874	565.3	3.7	0.85	0.3	0.5	3.1	−0.2	15

Lattice parameters for powder GaN [22]; $a_0^{GaN} = 0.31891$ nm; $c_0^{GaN} = 0.51855$ nm

Frequency of the E_2 (high) phonon mode in the relaxed GaN [20]; 566.2 cm^{-1}

concentration level and type of point defects) of the crystal lattice in this layer. Therefore, ε_a and ε_c strain components in the GaN epilayers are the superposition of biaxial and hydrostatic strains [18, 21, 22].

$$\varepsilon_a = \varepsilon_a^{(b)} + \varepsilon_h \tag{3a}$$

$$\varepsilon_c = \varepsilon_c^{(b)} + \varepsilon_h \tag{3b}$$

$$\varepsilon_h = \frac{1-v}{1+v}\left(\varepsilon_c + \frac{2v}{1-v}\varepsilon_a\right) \tag{4a}$$

$$v = \frac{c_{13}}{c_{13} + c_{33}} \tag{4b}$$

In Eqs. (3a) and (3b) ε_h is the hydrostatic strain, $\varepsilon_c^{(b)}$ and $\varepsilon_a^{(b)}$ are the biaxial strains in the c- and a-direction, respectively. On the other hand, the parameters in Eqs. (4a) and (4b) are defined as; v is the Poisson ratio, and c_{13} and c_{33} are the elastic constants of the hexagonal GaN. The elastic constant values of the c_{13} and c_{33} in Eq. (4b), calculated by Brillouin scattering measurements [23], used as $c_{13} = 106$ GPa and $c_{33} = 398$ GPa and v were calculated as 0.21. The data for these Poisson ratio and the measured strains in-plane and out-of-plane strains were substituted into Eqs. (3a), (3b) and (4b), and the vertical ($\varepsilon_c^{(b)}$) and horizontal ($\varepsilon_a^{(b)}$) biaxial strain components and the hydrostatic strain (ε_h) were calculated. The calculated results are listed in Table 1.

The stresses in the HR-GaN/buffer/SiC structures originating from the mismatch between the lattice parameters of the epilayers and the substrate are biaxial [17, 18, 21, 22]. The in-plane biaxial stress in the GaN epilayer can be determined using the formula given below;

$$\sigma_f = M_f \varepsilon_a^{(b)} \tag{5}$$

$$M_f = c_{11} + c_{12} - \frac{2c_{13}^2}{c_{33}} \tag{6}$$

In Eq. (5), σ_f is the biaxial stress in film, M_f is the biaxial elastic modulus for a material with hexagonal crystal lattice structures strained in the [0001] crystallographic direction [23] and the $\varepsilon_a^{(b)}$ is the biaxial strain in the a-direction.

The values for the elastic constant of the hexagonal GaN crystal in Eq. (6) were taken as; $c_{11} = 390$ GPa, $c_{12} = 145$ GPa, $c_{13} = 106$ GPa, $c_{33} = 398$ GPa. After substitutions of the c_{ij} parameters in Eq. (6), the value for the biaxial elastic modulus was obtained as 478.5 GPa. The biaxial stress component in the crystallographic b-direction equals the component in the a-direction, whereas the biaxial stress component in the c-direction equals zero. The σ_f values were calculated by substituting the values of biaxial strain in the a-direction and the biaxial elastic modulus value in Eq. (5). The results for the σ_f are tabulated in Table 1.

Table 2 The mosaic structure parameters including the mean tilt angle, α_{tilt} and mean twist angle, α_{twist}, vertical coherence length, $L_\perp$, lateral coherence length, $L_{//}$, vertical heterogeneous strain, $\varepsilon_\perp$ and screw, edge type dislocation density in the HR-GaN epilayer that were grown on SiC substrate with different buffer structures are listed

Sample ID	HR-GaN epilayer						
	$\alpha_{twist} \pm 0.001$ (°)	$\alpha_{tilt} \times 10^{-3}$ (°) $\pm 2 \times 10^{-4}$ (°)	$L_{//} \pm 0.1$ (nm)	$L_\perp \pm 0.15$ (nm)	$\varepsilon_\perp (10^{-4}) \pm 1 \times 10^{-5}$	Screw type dislocation density, $D_{screw} \times 10^8 \pm 1 \times 10^{10}$ cm^{-2}	Edge type dislocation density, $D_{edge} \times 10^8 \pm 2 \times 10^{10}$ cm^{-2}
Sample A	0.153	1.6	5164.0	35.7	−3.3	1.03	7.75
Sample B	0.292	1.9	23377.2	28.4	−4.3	1.65	28.40
Sample C	0.120	1.1	661.7	65.9	−1.6	0.33	4.85
Sample D	0.133	1.0	2346.3	46.2	−2.8	0.61	5.87

According to the group theory, hexagonal wurtzite GaN structures belongs to the point group C_{6v} (6 mm) with four atoms per unit cell, and thus, group-theory analysis predicts that at the zone-center three is eight phonon modes. These modes are the two E_2 (E_2 (low) and E_2 (high)), one A_1 (TO), one A_1 (LO), one E_1 (TO), one E_1 (LO), as well as two B_1 (B_1 (low) and B_1 (high)) modes. The E_2 modes are Raman active, the A_1 and E_1 modes are both Raman and infrared active, but the two B_1 modes are silent [20, 24–26].

Raman spectra of the HR-GaN epilayers grown on 6H-SiC substrate with different buffer structures were recorded at room temperature. Figure 5a displays the Raman spectra of the all samples. As shown in Fig. 5a, in the backscattering geometry measurements, the allowed E_2 (high) and the A_1 (LO) phonon modes of the c-direction oriented GaN and the E_2 (TA), A_1 (LA), E_2 (TO) and A_1 (LO) phonon modes of the 6H-SiC substrate are can be seen and it is consistent with published results in the literature [26].

The E_2 (high) and A_1 (LO) phonon modes in the HR-GaN epilayers are given in Fig. 5a, b. The E_2 (high) modes are observed at 566.6, 566.1, 566.0 and 565.3 cm^{-1} for sample A, B, C and D, respectively (Table 1). In addition, the A_1 (LO) peaks located at 733, 732.5, 732.5, and 732 cm^{-1} for sample A, B, C and D, respectively. It can be seen that the Raman peaks for the 6H-SiC substrate occupy the same position for all the samples (Fig. 5a). However, there is a very small shift in the frequency of both E_2 (high) and A_1 (LO) phonon modes of HR-GaN epilayers. This is the results of the presence of very small strain in the HR-GaN epilayers.

The Raman frequency shift of the E_2 (high) phonon mode is sensitive to case of biaxial (0001)-plane oriented stress and it can be used to characterize the stress state in GaN epilayer [20, 24, 25]. The E_2 (high) phonon mode positions and their full width at half maximum (FWHM) for all samples are summarized in Table 1. One can see that there is a small difference in the E_2 (high) phonon mode position in the samples are within the range of fluctuation (565.3–566.6 cm^{-1}) by effect of small strain in GaN epitaxial layers. The frequency of the E_2 (high) phonon mode of 566.2 cm^{-1} is considered to be a precise frequency value for E_2 (high) phonon modes in the unstrained GaN layers [20]. The measured frequency values of the E_2 (high) modes for all samples are close to the stress-free GaN and correlated with the strain calculated with XRD measurements. It confirms that all the HR-GaN epilayers are under the very low strain. On the other hand, FWHM of the E_2 (high) phonon modes are changes between 3.3 and 4.9 cm^{-1}. The relative intensity and FWHM of the E_2 (high) modes are comparable to the published Raman spectra of high quality GaN [20, 24, 25].
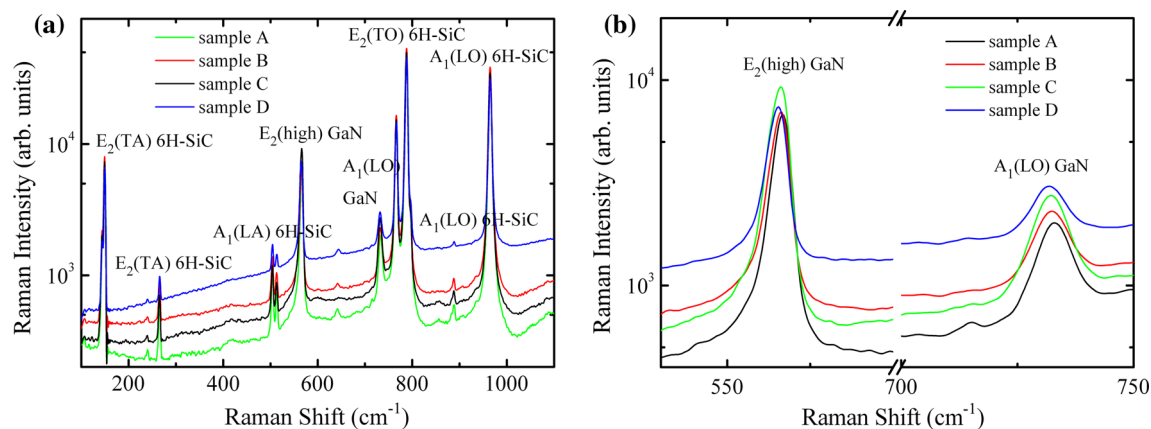
Fig. 5 **a** Raman spectra obtained at T = 300 K for the HR-GaN epilayers grown on 6H-SiC substrate with different buffer structures, for back scattering (surface) geometry ($\bar{z}(x,x)z$). **b** E_2 (high) and A_1(LO) phonon modes in the HR-GaN epilayers

The growth of the GaN based materials on the lattice mismatched substrate such as; sapphire, SiC and Si, causes threading dislocations in the GaN based epilayers. Generally, threading dislocation in the GaN based materials causes' destructive effects on devices that fabricated on these materials. In order to decrease threading dislocations some type of sophisticated buffer structures such as; low-temperature growth AlN, high-temperature growth AlN, AlN/GaN super lattice, AlGaN interlayer or combination of these layers have been used [18, 19]. These buffer systems can be considerably decreased threading dislocations but it could not completely quench [18, 19]. There are three types of dislocations present in the structures; the pure edge dislocation with Burgers vector of $b = \langle 11{-}20 \rangle/3$ ($\langle a \rangle$), the pure screw dislocation with Burgers vector of $b = \langle 0001 \rangle$ ($\langle c \rangle$), and the mixed dislocation with Burgers vector $b = \langle 11{-}23 \rangle/3$ ($\langle c + a \rangle$) [17, 19, 27–29]. The edge (D_{edge}) and screw (D_{screw}) type dislocation density in the epitaxial layers can be calculated by using the equation given below;

$$D_{screw} = \beta^2_{(0002)} \Big/ 9b^2_{screw} \qquad (7)$$

$$D_{edge} = \beta^2_{(10-12)} \Big/ 9b^2_{edge} \qquad (8)$$

In the Eqs. (7) and (8), β_{0002} and β_{10-12} are the FWHM of the (0002) symmetric and (10–12) asymmetric plane reflections measured by XRD rocking curves, respectively. The $b_{screw} = 0.5185$ nm and $b_{edge} = 0.3189$ nm are the Burgers vector lengths of screw components and edge components of the dislocations in the GaN epilayers, respectively [17, 19, 27–29]. The overall TDDs (D_{dis}) of the structures can be estimated by summation of D_{edge} and D_{screw} equation. The screw and edge type dislocation density of the HR-GaN epilayers, grown on different buffer structures, were calculated by using FWHM of the XRD rocking curves of (0002) symmetric and (10–12) asymmetric reflections. The calculated screw, edge type and

total dislocations densities in the HR-GaN by considering the errors are listed in Table 2.

As tabulated in Table 2, the screw type dislocation density in HR-GaN epilayers changes between 0.33×10^8 cm^{-2} (sample C) and 1.65×10^8 cm^{-2} (sample B), but edge type dislocation densities are a little bit higher than screw type dislocation densities and changes between 4.85×10^8 cm^{-2} (sample C) and 28.40×10^{-8} cm^{-2} (sample B). On the other hand, both screw and edge type dislocation densities in sample C are higher than sample A, B, and D.

The structure of the GaN epilayers is formed by slightly misoriented subgrains that form a mosaic structure, which is characterized by the nucleation of slightly misoriented islands and the coalescence of these islands toward a smooth surface [17, 19, 27–37]. The lateral ($L_{\parallel}$) and vertical ($L_{\perp}$) correlation length, heterogeneous strain ($\varepsilon_{\perp}$), and degree of mosaicity expressed by the mean tilt angle (α_{tilt}) and mean twist angle (α_{twist}) are important parameters in characterizing the quality of the epitaxial layers [17, 19, 27–37]. The out-of-plane rotation perpendicular to the surface normal and in-plane rotation around the surface normal of the mosaic blocks are defined as mean tilt and mean twist angle of the mosaic blocks, respectively [27–33]. The average absolute values of the tilt and twist angle are directly related to the FWHMs of the corresponding distributions of crystallographic orientations [27–34].

The Williamson–Hall (W–H) technique are the most used powerful technique in the calculation of the mosaic structure parameters of lateral and vertical coherence length, mean tilt angle and heterogeneous strain along the c-axis. Also, the mean twist angles can be determined by using some complicated calculation, fitting method or from direct measurement [33–36]. In the W–H technique, the broadening of the rocking curve in ω-scan (angular-scan)

of the (0002), (0004), and (0006) symmetric reflections for the epitaxial layers are influenced only by the α_{tilt} and short coherence length which parallel to the substrate surface [28, 29]. On the other hand, small $L_{\perp}$ and small $\varepsilon_{\perp}$ along the c-axis causes a broadening of the Bragg reflections in the radial-scan (ω-2θ scan) direction of the symmetric reflections. The mean α_{tilt} and $L_{\parallel}$ values of the materials can be derived from the W–H plot of $(FWHM)_{\omega\text{-scan}}(\sin\theta)/\lambda$ function against $(\sin\theta)/\lambda$ function for ω-scan of (0002), (0004), and (0006) symmetric reflections. The slope of the linear dependence is equal to the α_{tilt} and the inverse of the y-intersection y_o ($L_{\parallel} = 0.9/(2y_0)$) of the fitted line gives $L_{\parallel}$. In the function expression, $(FWHM)_{\omega\text{-scan}}$ is in the angular unit, θ is the Bragg reflection angle, and λ is the x-ray wavelength.

In addition, the plot of the $(FWHM)_{\omega\text{-}2\theta}(\cos\theta)/\lambda$ function against $(\sin\theta)/\lambda$ function is used in the $L_{\perp}$ and $\varepsilon_{\perp}$ calculation procedure. At that plot, the $(FWHM)_{\omega\text{-}2\theta}$ $(\cos\theta)/\lambda$ function against $(\sin\theta)/\lambda$ function is plotted for symmetric reflections, and gives straight line. The $L_{\perp}$ and $\varepsilon_{\perp}$ are estimated from the y-intersection y_0 ($L_{\perp} = 0.9/(2y_0)$) and the directly from the slope of the line, which is equal to the $4\varepsilon_{\perp}$, respectively [28, 29].

The W–H plots for symmetric plane reflections of the HR-GaN epilayers for the triple-axis (a) ω-scan and (b) ω-2θ-scan are demonstrated in Fig. 6a, b. The expected linear behavior of the graphs is experimentally well confirmed, which gives the rather accurate tilt angle values. But the slope of the W–H plots for ω-scan and ω-2θ-scan are different. The slopes of the plot of $(FWHM)_{\omega\text{-}2\theta}(\cos\theta)/\lambda$ against $(\sin\theta)/\lambda$ are negative in Fig. 6b. This behavior can be attributed to the compressive characteristic of the strain in the HR-GaN epilayers.

The measured α_{tilt} and $L_{\parallel}$ values of the HR-GaN epilayers for all samples are tabulated in Table 2. The mean α_{tilt} values of the samples changes between the 1.0×10^{-3} and 1.9×10^{-3} degree. As can be seen, the mean tilt angles of the HR-GaN epilayers for all the samples, except sample B, were similar to each other and rather small. It can be seen in this table that the mean tilt angle for the sample B is the higher than other samples. The $L_{\parallel}$ of the HR-GaN epilayers were determined to range from 661.7 to 23377.2 nm. The $L_{\parallel}$ is larger for HR-GaN epilayers grown on LT-AlN/HT-AlN buffer layers (23377.2 nm). On the other hand, smallest values for $L_{\parallel}$ calculated for sample c with LT-AlN/AlGaN buffer layers (661.7 nm). The maximum $L_{\parallel}$ values were measured for sample B and the minimum values obtained for sample C.

The measured $L_{\perp}$ and $\varepsilon_{\perp}$ values for HR-GaN epilayers are listed in Table 2. The $L_{\perp}$ values for HR-GaN epilayers range from 35.7 (sample A) to 65.9 nm (sample C). On the other hand, the negative $\varepsilon_{\perp}$ values obtained for the HR-GaN epilayers for all samples. These negative values can be attributed to the compressive characteristic of the strain in HR-GaN epilayers. The maximum and the minimum values for $\varepsilon_{\perp}$ in the HR-GaN epilayers were measured as -4.3×10^{-4} and -1.6×10^{-4} for sample B and sample C, respectively.

In the last decade, several direct and indirect techniques have been published in the literature about the mean twist angle determination [29, 32–37]. Some of the authors used a geometrical model that considers the simultaneous presence of tilt and twist to fit the data from the measurement of ω-scans in skew geometry from reflections with increasing lattice plane inclination. In their twist angle measurements methods, they used more complicated
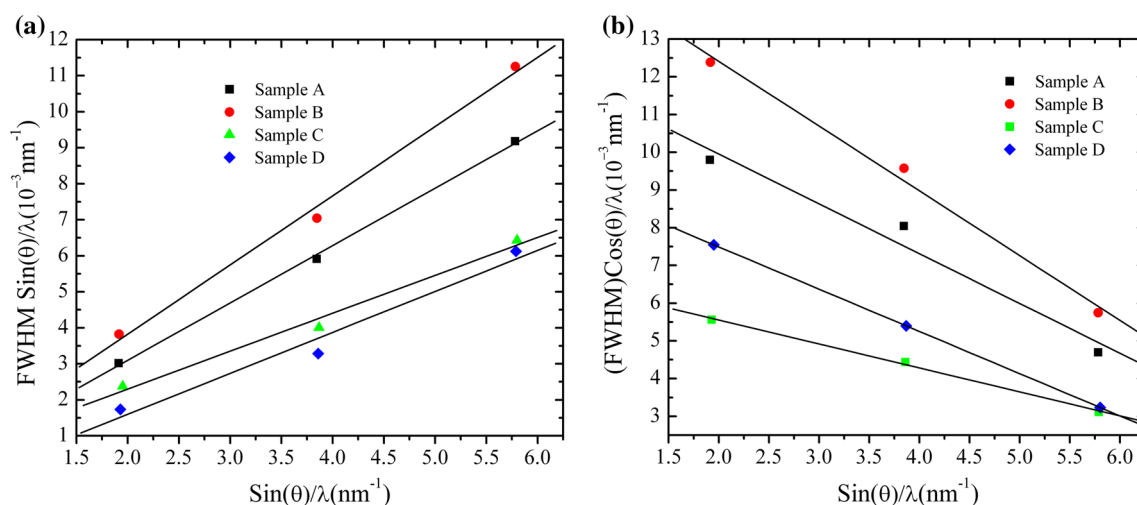
Fig. 6 W–H plot for GaN epilayers. a Triple-axis ω scan and b triple-axis ω-2θ scan were measured for the symmetric (000l) ($l = 2, 4, 6$) reflections indicated in the figure. The *lines* result from a linear fit to the experimental data

calculation and fitting procedures [30, 31]. On the other hand, some authors proposed a simple empirical approach to obtain the mean twist angle directly without using complicated computation and fitting procedure [35, 36].

The FWHM of ω-scan or Φ-scan of the XRD measurements can be used for the determination of the mean twist angle between the mosaic blocks [18, 29, 31–37]. The FWHM of the rocking curve of an imperfect film is composed of several contributions, such as the mean tilt, twist, the average size of the sub-grains, and the inhomogeneous strain distributions. The α_{twist} can be extrapolated from a fit to the measured double-axis scans data for different (hkl) reflections in a skew symmetric diffraction. Many others report in the literature about the extrapolation and direct measurements methods for the α_{twist} determination [29, 32–37]. In this report, the authors used a geometrical model that considers the simultaneous presence of tilt and twist to fit the data from the measurement of ω-scans in skew geometry from reflections with increasing lattice plane inclination. In their model, they used some complicated calculation and fitting method. On the other hand, some authors proposed a simple empirical approach to obtain the α_{twist} directly without falling into a complicated computation and fitting procedure [32–36]. In our study, we measured the mean twist angles of the AlN epilayers directly by using simple empirical approach.

In the our measurements, in order to eliminate the broadening due to the domain size and inhomogeneous strain effect, we have used a slit of 0.6 mm in front of the detector in double-axis ω-scans. In the actual case, their contribution to the overall broadening was found to be of minor influence. Another important point for the direct measurements is that the intrinsic width of the reflection for the crystal and the apparatus broadening for all the experimental reflections are negligible because these effects amount to only a few arcsec. In addition, the (0002) reflection and ($hk(-h-k)l$) reflections with either h or k non-zero orientation of our samples with triple-axis ω-2θ scans, exhibit a small FWHM. For this reason, we can only measure the broadening that was caused by the twist using ($hk(-h-k)l$) reflections in skew geometry [29, 32, 33].

The FWHMs values of the ω and Φ-scans of the (10–15), (10–14), (10–13), (10–12), (20–23), (11–22), (20–21), (12–31) plane reflections with respect to inclination angle (χ) for measured in sample D are given in Fig. 7. The FWHMs of ω-scans increase with the increment of χ, while the FWHM of Φ scan decrease with the increment of χ angle. Moreover, they become closer when the (12–31) reflection yields at 78.6° in χ as shown in Fig. 7. In fact, the angle χ reaches 90° when the reflection plane is perpendicular to the surface of the sample. At that χ angle values, the mean twist angle of the mosaic block is close to the FWHM of the rocking-curve of ω or Φ-scans. In every
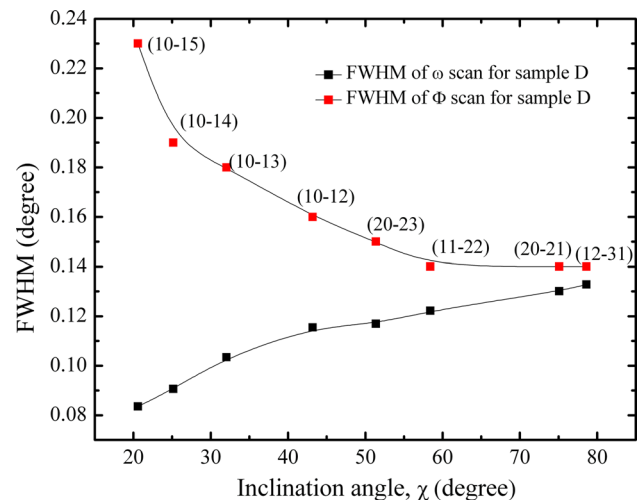
Fig. 7 FWHM of Φ and ω scans for ($hk(-h-k)l$) reflections as a function of the inclination angle χ for sample D. The FWHMs of ω-scan increase with the increment of χ angle, while those of Φ scan decrease. The *lines* are a guide for the eyes

respect, the FWHMs of Φ-scans are larger than those of ω-scans with the change of the χ. Therefore, the mean twist angles must be equal to the average value of the FWHMs of ω and Φ-scans at inclination angle of 78.6°.

The calculated values of the mean twist angles of the HR-GaN epilayers are tabulated in Table 2. The α_{twist} values changes between 0.120° and 0.292° and the α_{twist} values for the HR-GaN epilayers of the all samples are different. The biggest mean twist angle value (0.292°) obtained for sample B and is approx. two times higher than other samples. Based on this observation, it can be argued that the α_{twist} of the HR-GaN epilayers grown on 6H-SiC substrate strongly affect the buffer structures in our case.

4 Conclusions

In the present study, HR-GaN epilayers, with different buffer structures, were grown on 6H-SiC substrate by MOCVD. The resistivities of the GaN epilayers are on the order of 10^8 Ω cm. The strain behaviors in the HR-GaN epilayers were estimated using XRD and Raman measurements. Both XRD and Raman results confirmed that there is low residual stress in the HR-GaN epilayers for all samples. Based on the XRD measurement, the strain values in the HR-GaN epilayers in sample C and D are one order small than sample A and B. The mosaic structures parameters (such as lateral and vertical coherence lengths, tilt and twist angle and heterogeneous strain) and dislocation densities (edge and screw dislocations) and the residual stress of the HR-GaN epilayers grown on different buffer structures were investigated using XRD measurements. Results show that the mosaic structures parameters,

lateral and vertical coherence lengths, tilt and twist angle, and strains of the HR-GaN epilayers were affected by buffer structures.

References

1. H. Morkoç, *Nitride Semiconductors and Devices* (Springer, Heidelberg, 1999)
2. S. Nakamura, G. Fasol, *The Blue Laser Diode—GaN Based Light Emitters and Lasers* (Springer, Heidelberg, 1997)
3. R.S. Pengelly, S.M. Wood, J.W. Milligan, S.T. Sheppard, W.L. Pribble, IEEE Trans. Microw. Theory Tech. **60**(6) (2012)
4. M.J. Uren, J. Möreke, M. Kuball, IEEE Trans. Electron. Devices **59**, 3327 (2012)
5. P.B. Klein, S.C. Binari, K. Ikossi, A.E. Wickenden, D.D. Koleske, R.L. Henry, Appl. Phys. Lett. **79**, 3527 (2001)
6. Z. Chen, Y. Pei, S. Newman, R. Chu, D. Brown, R. Chung, S. Keller, S.P. Denbaars, S. Nakamura, U.K. Mishra, Appl. Phys. Lett. **94**, 112108 (2009)
7. M. Rudziński, V. Desmaris, P.A. van Hal, J.L. Weyher, P.R. Hageman, K. Dynefors, T.C. Rödle, H.F.F. Jos, H. Zirath, P.K. Larsen, Phys. Status Solidi C **3**(6), 2231–2236 (2006)
8. G. Callsen, M.R. Wagner, T. Kure, J.S. Reparaz, M. Bugler, J. Brunnmeier, C. Nenstiel, A. Hoffmann, M. Hoffmann, J. Tweedie, Z. Bryan, S. Aygun, R. Kirste, R. Collazo, Z. Sitar, Phys. Rev. B **86**, 075207 (2012)
9. C.H. Seager, A.F. Wright, J. Yu, W. Götz, J. Appl. Phys. **92**, 6553 (2002)
10. M.E. Twigg, D.D. Koleske, A.E. Wickenden, R.L. Henry, S.C. Binari, Appl. Phys. Lett. **79**, 4322 (2001)
11. Jr-T. Chen, U. Forsberg, E. Janzen, Appl. Phys. Lett. **102**, 193506 (2013)
12. A.E. Wickenden, D.D. Koleskel, R.L. Henry, M.E. Twigg, M. Fatemi, J. Cryst. Growth **260**, 54–62 (2004)
13. Y. Kokubun, J. Nishio, M. Abe, T. Ehara, S. Nakagomi, J. Electron. Mater. **30**, 23 (2001)
14. Z. Zhong-Tang, G. Li-Wei, X. Zhi-Gang, D. Guo-Jian, Z. Jie, P. Ming-Zeng, J. Hai-Qiang, C. Hong, Z. Jun-Ming, Chin. Phys. Lett. **24**(6), 1641 (2007)
15. S.M. Hubbard, G. Zhao, D. Pavlidis, W. Sutton, E. Cho, High-resistivity GaN buffer templates and their optimization for GaN-based HFETs (SAFİR ÜZERİNE). J. Cryst. Growth **284**, 297–305 (2005)
16. P. Waltereit, O. Brandt, A. Trampert, M. Ramsteiner, M. Reiche, M. Qi, K.H. Ploog, Appl. Phys. Lett. **74**, 3660 (1999)
17. M.A. Moram, M.E. Vickers, Rep. Prog. Phys. **72**, 036502 (2009)
18. M.K. Ozturk, E. Arslan, İ. Kars, S. Ozcelik, E. Ozbay, Mater. Sci. Semicond. Process. **16**, 83 (2013)
19. E. Arslan, M.K. Ozturk, H. Çakmak, P. Demirel, S. Özçelik, E. Ozbay, J. Mater. Sci. Mater. Electron. **24**, 4471 (2013)
20. C. Kisielowski, J. Kruger, S. Ruvimov, T. Suski, J.W. Ager III, E. Jones, Z. Liliental-Weber, M. Rubin, E.R. Weber, M.D. Bremser, R.F. Davis, Phys. Rev. B **54**, 17745 (1996)
21. D.J. Dunstan, J. Mater. Sci. Mater. Electron. **8**, 337 (1997)
22. C.M. Balkas, C. Basceri, R.F. Davis, Powder Diffr. **10**, 266–268 (1995)
23. A. Polian, M. Grimsditch, I.G. Grzegory, J. Appl. Phys. **79**, 3343 (1996)
24. V.Y. Davydov, Y.E. Kitaev, I.N. Goncharuk, A.N. Smirnov, J. Graul, O. Semchinova, D. Uffmann, M.B. Smirnov, A.P. Mirgorodsky, R.A. Evarestov, Phys. Rev. B **58**, 12899 (1998)
25. H. Harima, J. Phys. Condens. Matter **14**, R967–R993 (2002)
26. S. Nakashima, H. Harima, Phys. Status Solidi A **162**, 39 (1997)
27. B. Heying, X.H. Wu, S. Keller, Y. Li, D. Kapolnek, B.P. Keller, S.P. DenBaars, J.S. Speck, Appl. Phys. Lett. **68**(5), 643 (1996)
28. V.M. Kaganer, O. Brandt, A. Trampert, K.H. Ploog, Phys. Rev. B **72**, 045423 (2005)
29. T. Metzger, R. Höppler, E. Born, O. Ambacher, M. Stutzmann, R. Stömmer, M. Schuster, H. Göbel, S. Christiansen, M. Albrecht, H.P. Strunk, Philos. Mag. A **77**, 1013 (1998)
30. G.K. Williamson, W.H. Hall, Acta Metall. **1**, 22 (1953)
31. V. Holy, J. Kubena, E. Abramof, K. Lischka, A. Pesek, E. Koppensteiner, J. Appl. Phys. **74**, 1736 (1993)
32. R. Chierchia, T.B. Wttcher, H. Heinke, S. Einfeldt, S. Figge, D. Hommel, J. Appl. Phys. **93**, 8918 (2003)
33. V. Srikant, J.S. Speck, D.R. Clarke, J. Appl. Phys. **82**, 4286 (1997)
34. Y.J. Sun, O. Brandt, T.Y. Liu, A. Trampert, K.H. Ploog, J. Blasing, A. Krost, Appl. Phys. Lett. **81**, 4928 (2002)
35. X.H. Zheng, H. Chen, Z.B. Yan, Y.J. Han, H.B. Yu, D.S. Li, Q. Huang, J.M. Zhou, J. Cryst. Growth **255**, 63 (2003)
36. H. Li, Y. Luo, L. Wang, G. Xi, Y. Jiang, W. Zhao, Y. Han, Appl. Phys. Express **1**, 045004 (2008)
37. J.Q. Liu, J.F. Wang, Y.X. Qiu, X. Guo, K. Huang, Y.M. Zhang, X.J. Hu, Y. Xu, K. Xu, X.H. Huang, H. Yang, Semicond. Sci. Technol. **24**, 125007 (2009)